ACS OMEGA

http://pubs.acs.org/journal/acsodf

Article

Influence of Ag Metal Dispersion on the Catalyzed Reduction of CO_2 into Chemical Fuels over Ag−ZrO_2 Catalysts

Ruonan Duan, Wu Qin, Xianbin Xiao, Bingyun Ma, and Zongming Zheng*

Cite This: *ACS Omega* 2022, 7, 34213−34221

Read Online

ACCESS | Metrics & More | Article Recommendations | Supporting Information

ABSTRACT: Metal/metal oxide catalysts reveal unique CO_2 adsorption and hydrogenation properties in CO_2 electroreduction for the synthesis of chemical fuels. The dispersion of active components on the surface of metal oxide has unique quantum effects, significantly affecting the catalytic activity and selectivity. Catalyst models with 25, 50, and 75% Ag covering on ZrO_2, denoted as $Ag_4/(ZrO_2)_9$, $Ag_8/(ZrO_2)_9$, and $Ag_{12}/(ZrO_2)_9$, respectively, were developed and coupled with a detailed investigation of the electronic properties and electroreduction processes from CO_2 into different chemical fuels using density functional theory calculations. The dispersion of Ag can obviously tune the hybridization between the active site of the catalyst and the O atom of the intermediate species CH_3O^* derived from the reduction of CO_2, which can be expected as the key intermediate to lead the reduction path to differentiation of generation of CH_4 and CH_3OH. The weak hybridization between CH_3O^* and $Ag_4/(ZrO_2)_9$ and $Ag_{12}/(ZrO_2)_9$ favors the further reduction of CH_3O^* into CH_3OH. In stark contrast, the strong hybridization between CH_3O^* and $Ag_8/(ZrO_2)_9$ promotes the dissociation of the C−O bond of CH_3O^*, thus leading to the generation of CH_4. Results provide a fundamental understanding of the CO_2 reduction mechanism on the metal/metal oxide surface, favoring novel catalyst rational design and chemical fuel production.

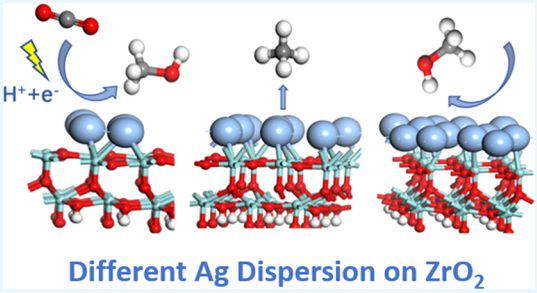

1. INTRODUCTION

To curb atmospheric CO_2 levels while producing valuable products, researchers have developed many techniques for capturing and recycling CO_2.[1−3] Among various utilization methods, electrocatalytic reduction of CO_2 technology coupled with renewable energy power systems has been of wide concern due to its energy consumption and economic advantages.[4] This technology can use CO_2 and renewable energy power as inexpensive raw materials for the production of chemical fuels, thus allowing CO_2 to be recycled as the energy-carrying compound.[5−11] The main problems of electrocatalytic reduction of CO_2 are the required high overpotential, insufficient catalyst performance, and poor selectivity.[12] The optimization of catalytic performance lies in the improvement of the electrocatalyst, which plays the role of providing binding sites for CO_2, activating CO_2, and stabilizing reaction intermediates in the reaction process.[13] A variety of catalyst modification methods were adopted to manipulate catalysis, including bimetal alloys,[14,15] metal oxides,[16,17] metal−organic framework complexes,[18,19] metal-free carbon-based catalysts,[20,21] and so forth. Metal oxide catalysts[16,22−24] exhibit great catalytic properties such as high selectivity and Faradaic efficiency, which may be attributed to oxidized metal species and metal oxide interactions that promote the activation of CO_2 and stabilization of intermediates.[25,26] Fabricating composites by introducing foreign metal species to metal oxides is conducive to achieving enhanced performance in CO_2 reduction. Fan and Fujimoto[27] reported the strong metal support interaction between Pd and CeO_2 support materials, which makes the catalyst more electronegative than pure Pd catalysts. The interaction enhances the hydrogenation activity of carbonyl bonds, prolongs the lifetime of electrocatalysts, and favors methanol production. Graciani et al.[28] put Cu particles on CeO_2 to facilitate the conversion to methanol. The unique synergistic effect between metals and oxides can be reflected in the appearance of electronic disturbances in the metal after loading on the metal oxides. Meanwhile, oxides also act as support materials to stabilize catalysts and provide preferable electron conduction and species transport for the reduction process.[29,30] Duyar et al.[31] found that ZrO_2 has the striking ability to modify formate binding, and therefore, the MoP/ZrO_2 catalyst can shift the selectivity toward methanol of 55.4%.

It would be desirable to minimize the amount of expensive silver used in the catalyst while maintaining a high selectivity for target products. Loading a moderate number of Ag atoms on oxide enhances the promise of these catalysts for the economic reduction of CO_2. Zhu et al.[32] reported the positive

Received: June 8, 2022
Accepted: September 1, 2022
Published: September 14, 2022

https://doi.org/10.1021/acsomega.2c03587
ACS Omega 2022, 7, 34213−34221

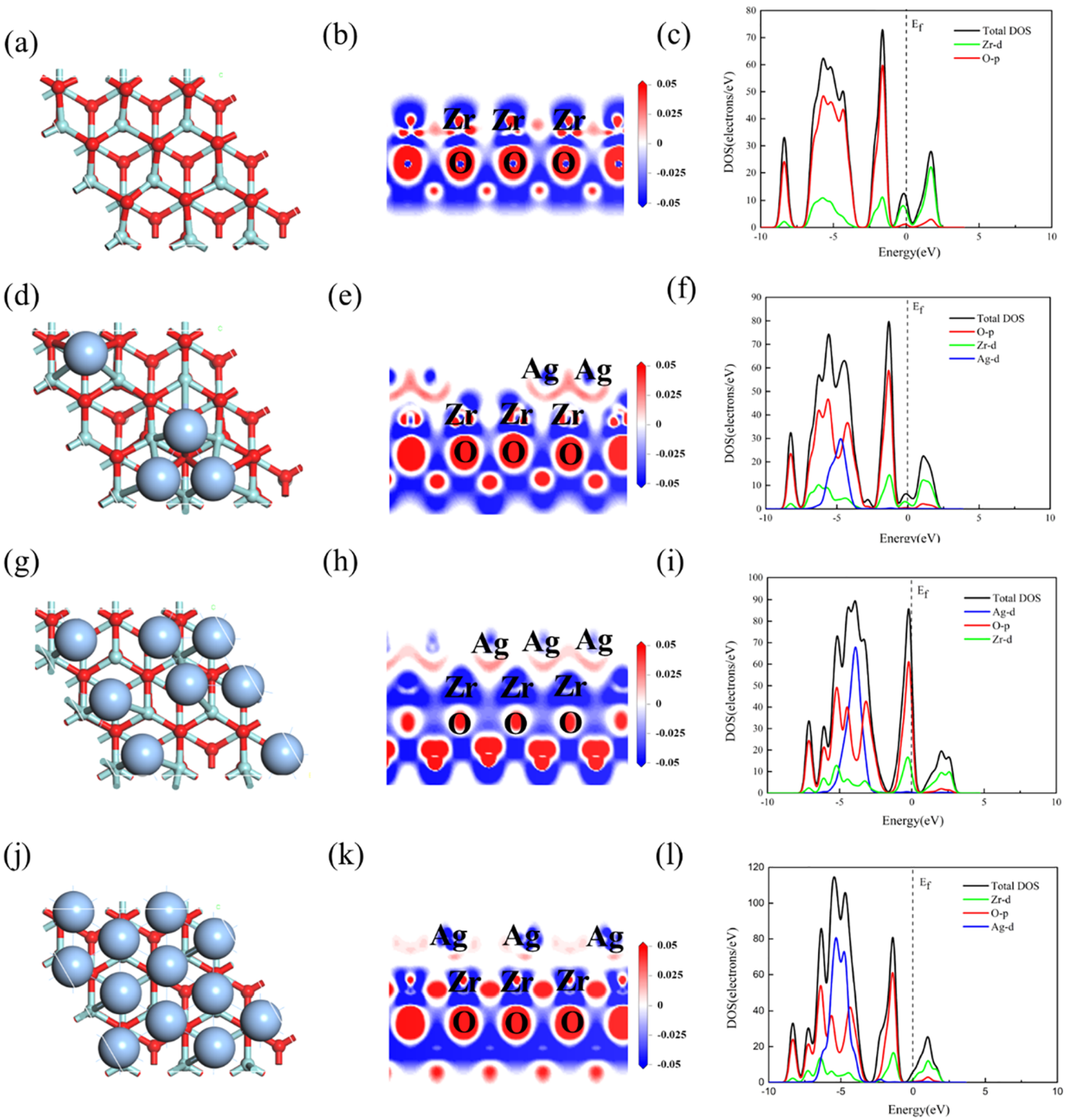

Figure 1. Top view of configuration, difference charge density, and density of states of (a–c) ZrO_2, (d–f) $Ag_4/(ZrO_2)_9$, (g–i) $Ag_8/(ZrO_2)_9$, and (j–l) $Ag_{12}/(ZrO_2)_9$ models. The blue, red, and green spheres indicate silver, oxygen, and zirconium atoms, respectively. A loss of electrons is indicated in blue, while electron enrichment is indicated in red.

effect of the Cu/ZnO–CeO_2 catalyst prepared by flame spray pyrolysis. The 40 wt % Cu loading ZnO–CeO_2 catalyst with strong metal–oxide interactions displayed high CH_3OH selectivity due to a high formate coverage. Ma et al.[29] studied the effect of Ag loading on the Ag/TiO_2 catalyst: for the 5–40 wt % samples, the partial current density and Faradaic efficiency for CO increased with the number of Ag particles exposed on the TiO_2 surface. However, the transmission electron microscopy images suggested that Ag particles were prone to agglomeration in 60 wt % Ag/TiO_2, which may have led to unsatisfactory results. These instructive studies have explored the effect of active metal dispersion on catalytic performance, but there is still a lack of in-depth understanding of specific mechanisms. Therefore, this study reveals the influence mechanism of active metal dispersion on electron transport between the catalyst interface as well as CO_2 adsorption and reduction properties.

In this work, the electron transport between the Ag and ZrO_2 interface was investigated to understand the metal–oxide interaction and synergetic effect. The adsorption energies and Gibbs free energies of different species in the synthesis of CH_3OH and CH_4 on Ag/ZrO_2 surfaces with different Ag

https://doi.org/10.1021/acsomega.2c03587
ACS Omega 2022, 7, 34213–34221

dispersion were analyzed through density functional theory (DFT) calculations. The binding ability of O* in key intermediates with the catalyst and the relation between Ag dispersion and O* binding ability were discussed to clarify how the ZrO_2 support and Ag dispersion have affected the catalytic process.

2. COMPUTATIONAL METHODS

All the calculations were performed in the framework of DFT[33] by using the DMOL[3] and CASTEP code with the generalized gradient approximation and Perdew–Burke–Ernzerhof functional[34] for exchange and correlation potentials. Geometry optimization and energy calculations were carried out using CASTEP with the plane wave ultrasoft pseudopotential approach. Spin polarization was considered throughout all calculations. The Pulay density mixing method was used with an energy convergence tolerance of 5.0×10^{-5} eV/atom. The force on every atom was smaller than 0.01 eV/nm. DMOL[3] with a DNP basis set performed frequency calculations to analyze vibration frequencies and electronic properties. The locate task with the Metropolis method and COMPASS forcefield in the sorption module were selected to determine the adsorption sites of Ag atoms on ZrO_2. A plane wave cutoff energy of 600 eV was applied. A combination of the linear synchronous transit and quadratic synchronous transit method[35] was employed to search the transition state of reactions. The adsorption energy (E_{ads}) was calculated as follows

$$E_{ads} = E_{adsorbate,surface} - E_{surface} - E_{adsorbate} \quad (1)$$

where $E_{adsorbate,surface}$, $E_{surface}$, and $E_{adsorbate}$ represent the total energies of the surface slabs with adsorbates, the bare slabs, and free molecules, respectively. A negative E_{ads} value indicates that the adsorption process is exothermic, whereas a positive value is for an endothermic process. By calculating reaction energies and activation barriers of elementary steps, we listed the most possible reaction pathways for CO_2 reduction on Ag/ZrO_2. The Gibbs free energies of different species were calculated from the computational hydrogen electrode proposed by Nørskov et al.[36] The Gibbs free energy of each reaction step was calculated as follows

$$G = E_{elec} + ZPE - TS \quad (2)$$

where E_{elec}, ZPE, T, and S represent the calculated energy of electron, zero-point energy, temperature, and entropy, respectively.

3. RESULTS AND DISCUSSION

3.1. Properties of Ag/ZrO_2 with Different Ag Surface Dispersion. The ZrO_2 model was imported from the structure file in the Materials Studio software package. A six-layer ZrO_2(111) slab was cleaved from a perfect ZrO_2 crystal with the top two layers being fully relaxed and the bottom three layers being fixed to simulate the catalyst surface. To eliminate spurious interference between periodic images, the vacuum thickness was set as 12 Å. To simulate the reaction environment in the electrolyte, the H atoms were adsorbed on the model to simulate the surface hydroxylation of the catalyst. The surface containing 36 O atoms, 18 Zr atoms, and 9 H atoms was expanded using a supercell of 10.76 × 10.76 × 17.85 Å. The sorption module was used to perform Ag adsorption calculation on the ZrO_2(111) surface. The calculation results show that when the number of single-layer Ag atoms adsorbed on the ZrO_2(111) surface reaches 16, the Ag dispersion is 100%. Figure 1 illustrates the most stable configurations for the Ag/ZrO_2 model with 25, 50, and 75% Ag dispersion, and the number of Ag atoms is 4, 8, and 12, respectively. The front views of the models are displayed in Figure S1. For the convenience of description, $Ag_4/(ZrO_2)_9$, $Ag_8/(ZrO_2)_9$, and $Ag_{12}/(ZrO_2)_9$ were used to represent 25, 50, and 75% Ag atom dispersion models, respectively.

Due to the difference in the Fermi level between metal and oxide, the binding of metal and oxide results in the transfer of electrons to achieve the equilibrium of the Fermi level at the interface. The display of the density difference as a 2D slice in Figure 1 contributed to an understanding of the electron distribution process. The positions of the slices (parallel to the B and C axis) are provided in Figure S2. The density of states analysis was also adopted to further investigate the interaction of Ag and oxides, as shown in Figure 1.

As Figure 1b shows the difference charge density, O atoms in original ZrO_2 provide an electron-rich region, while Zr atoms provide a vacant orbital in the lattice. In Figure 1e,h,k, the existence of the enrichment region around the Ag atoms indicates the electron transfer from the oxide to Ag. The valence band is predominantly composed of O 2p states in pristine ZrO_2. After the introduction of Ag, the electronic states of the Ag 4d impurity appear at the top of the valence band and exhibit some energy dispersion. A stronger intensity of the electronic states of the Ag 4d impurity level is observed in higher-coverage Ag/ZrO_2. The splitting of the DOS peaks between −6 and −3 eV exhibited more energy dispersion as the number of Ag atoms increased, implying that more Zr atoms and O atoms contributed to the hybridization with Ag atoms; in the Ag_8/ZrO_2 system, the high densities of states near the Fermi energy indicated the promotion of electron transfer. The properties of Ag/ZrO_2 catalysts were further elucidated by calculating the charge transfer and binding energy of loaded Ag atoms, as shown in Table 1.

Table 1. Average Binding Energy of Ag Atoms on the Surface of Ag/ZrO_2 and Net Charges

structures	Ag dispersion (%)	binding energy per Ag atom (eV)	transferred net charges per Ag atom (|e|)
$Ag_4/(ZrO_2)_9$	25	−1.21	−0.18
$Ag_8/(ZrO_2)_9$	50	−0.97	−0.11
$Ag_{12}/(ZrO_2)_9$	75	−1.21	−0.05

The average binding energy of Ag atoms was not proportional to the dispersion of Ag atoms as shown in Table 1. Similar to the irregularity between different Au numbers and average binding energy on Au/ZrO_2 reported by Liang et al.,[37] the result demonstrated that the number of metal atoms affected the electronic structure of the catalyst interface and binding stability of the loaded metal. To further explain this behavior, the partial density of states of the Ag, Zr, and O atoms involved in Ag adsorption systems is displayed in Figure S3. In comparison to the $Ag_4/(ZrO_2)_9$ and $Ag_{12}/(ZrO_2)_9$ systems, the overlapping region near the Fermi level (−8 to −2 eV) due to Ag bonding with O and Zr atoms was slightly smaller for the $Ag_8/(ZrO_2)_9$ system, which indicated the weaker chemical bonding between the Ag and ZrO_2 in the $Ag_8/(ZrO_2)_9$ system.[38] According to Mulliken population

https://doi.org/10.1021/acsomega.2c03587
ACS Omega 2022, 7, 34213−34221

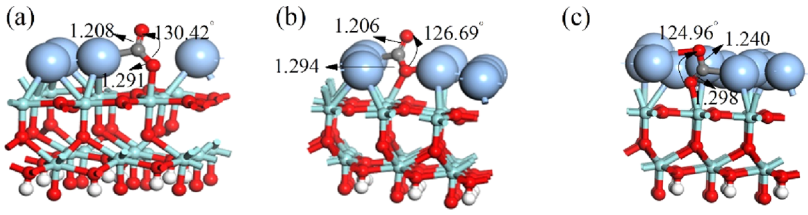

Figure 2. Most stable structures of CO_2 adsorption on (a) $Ag_4/(ZrO_2)_9$, (b) $Ag_8/(ZrO_2)_9$, and (c) $Ag_{12}/(ZrO_2)_9$. The blue, red, and green spheres indicate silver, oxygen, and zirconium atoms, respectively. The bond lengths are in units of Å.

analysis, the net charges of Ag atoms in Ag/ZrO_2 were lower than those on the original Ag surface after adsorption, indicating that electrons transferred from ZrO_2 to Ag. Meanwhile, the average number of electrons transferred to each Ag atom decreased with the increase in Ag atoms. We compared the up- and down-spin Ag s-orbital signature in pure Ag-atom systems with that of Ag atom in Ag/ZrO_2 systems (Figure S4). After the loading of Ag atoms on the ZrO_2 surface, the more parts of the signature due to the Ag s orbital appear below the Fermi level, showing the reduction of Ag atoms due to electron transfer from the ZrO_2 support. We also found some up- and down-spin states above the Fermi energy, which may be because of the anti-bonding of the Ag atoms with the Zr and O atoms.[39,40] Additionally, the visualization of the spin densities, as shown in Figure S5, of the Ag/ZrO_2 systems demonstrated that the Ag atoms became less positively charged after loading. In the Ag_8/ZrO_2 system, the spin densities with the d orbital of Zr atoms and the p-orbital characteristics of O atoms were found to be localized around the Ag atoms, evidencing the chemical bonding between Ag and ZrO_2. In the Ag_{12}/ZrO_2 system, in addition to the orbital properties of Zr and O atoms, the spin densities with d-orbital characteristics of Ag atoms were found to be more obvious than those of the Ag_8/ZrO_2 system, which also corresponds to the more stable adsorption of Ag atoms in the Ag_{12}/ZrO_2 system. The results displayed in Table 1 suggest that the Ag dispersion affects electron transfer at the Ag/ZrO_2 interface and the binding strength of Ag atoms, which plays a vital role in the subsequent CO_2 adsorption and reduction process.

3.2. Adsorption Properties of CO_2 on Ag/ZrO_2 Catalysts. Adsorption of CO_2 on the catalyst is one of the key steps in CO_2 electroreduction. The models in which CO_2 was only adsorbed on the Ag atomic layer or the ZrO_2 surface were constructed, but the higher adsorption energies indicated the unstable adsorption. Therefore, eight adsorption structures of Ag/ZrO_2 for CO_2 adsorption at Ag/ZrO_2 interfaces were considered as shown in Figure S6. The adsorption energies were investigated as shown in Table S1, and the structures with the lowest adsorption energies were chosen as the starting positions. For each catalyst surface, the most stable structures are shown in Figure 2.

Compared with the free-CO_2 molecule structure (the length of the C−O bond is 1.18 Å), the bond lengths of three adsorbed structures increased while the bond angles decreased, implying that CO_2 molecules were activated after adsorption.[41] Besides, the vibrational modes were investigated to further explore the activation of CO_2 (shown in Figure S7). The vibrational frequency modes of free CO_2 in the gas phase are asymmetric stretching (one bond contracts while the other elongates), symmetric stretching (two bonds contract or elongate synchronously), and in-/out-plane bending (O−C−O bond angle changes from 180°) modes. The calculated frequencies of 2383 (asymmetric stretching), 1331 (symmetric stretching), and 664 (bending) cm^{-1} are in good agreement with the experimental results of 2349, 1333, and 667 cm^{-1}.[42] All the asymmetric and symmetric stretching modes of bent CO_2 have lower frequencies. The strong red shifts for adsorbed CO_2 are due to the distinct strong interactions of the CO_2 molecule with the surface atoms. Table 2 lists the adsorption energies and Mulliken population analysis for Ag/ZrO_2 models.

Table 2. Adsorption Energies of CO_2 and Mulliken Charges of CO_2, Ag, and $ZrO_2(111)$

		net charges (|e|)		
		Ag	CO_2	$ZrO_2(111)$
structures	ΔE_{ads} (eV)	−0.7	0	0.7
$Ag_4/(ZrO_2)_9$	−0.59	−0.37	−0.66	1.03
$Ag_8/(ZrO_2)_9$	−0.03	−1.53	−0.64	2.17
$Ag_{12}/(ZrO_2)_9$	0.31	−1.96	−0.76	2.72

The adsorption energy of CO_2 increased with Ag dispersion, indicating that the catalyst with lower Ag dispersion stabilized CO_2 adsorption and favored subsequent reduction. On the Ag(111) catalyst without an oxide support, the net charges on CO_2 after adsorption were less than those on Ag/ZrO_2 catalysts. Besides, the number of electrons supplied by ZrO_2 increased with higher Ag dispersion. On $Ag_4/(ZrO_2)_9$, Ag and ZrO_2 both contributed to supply electrons to reduce CO_2, while on $Ag_8/(ZrO_2)_9$ and $Ag_{12}/(ZrO_2)_9$, ZrO_2 provided electrons to Ag and CO_2. The higher Ag dispersion decreases the stability of CO_2 adsorption while increases the number of electrons conducted to CO_2. The results underscore the important role of the ZrO_2 support and Ag dispersion in CO_2 adsorption and reduction, suggesting the synergistic effect between Ag and ZrO_2.

3.3. Energy Diagrams and Reduction Paths in CH_4 and CH_3OH Synthesis. The stable structure of CO_2 adsorption on the surface (denoted as CO_2^*) was used to study the CO_2 reduction. The first step of hydrogenation of CO_2^* may occur at the O or C atoms to form COOH* or HCOO* intermediates, respectively. Therefore, two possible CO_2 reduction paths were taken into account. Figure 3 shows the CO_2 reduction free energy diagram on the $Ag_4/(ZrO_2)_9$ catalyst and possible intermediates according to DFT calculation results.

On the pure Ag surface, the main path of CO_2 reduction is CO_2 → COOH* → CO* in most cases, leading to the generation of CO gas.[43,44] The reaction energy of COOH* forming CO* on the Ag(110) surface is −0.51 eV, while on the $Ag_4/(ZrO_2)_9$ surface, it is −1.17 eV. In addition, the adsorption energy of CO* on the $Ag_4/(ZrO_2)_9$ surface is 2.47 eV, which means that the desorption of CO* is difficult to

https://doi.org/10.1021/acsomega.2c03587
ACS Omega 2022, 7, 34213−34221

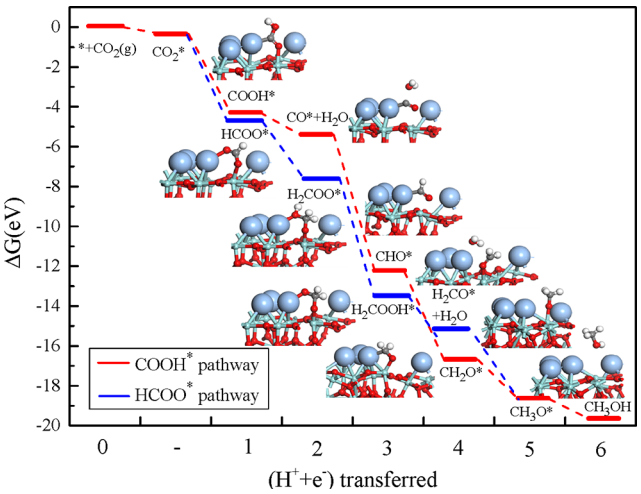

Figure 3. Free energy diagram of CO_2 reduction on $Ag_4/(ZrO_2)_9$ along COOH* and HCOO* pathways at 0 V (RHE). The red line represents the COOH* pathway, and the blue line represents the HCOO* pathway.

occur. Therefore, CO_2 can be further reduced to other products on $Ag_4/(ZrO_2)_9$, and the reaction can be carried out more thoroughly.

Another pathway for CO_2^* hydrogenation is through the HCOO* intermediate. After the formation of HCOO*, the intermediate is subsequently hydrogenated to H_2COO* and H_2COOH*, with the required barrier energies of 0.82 and 2.43 eV, respectively. Finally, CO_2 is reduced to CH_3OH. The barrier energy for COOH* is 0.734 eV, compared to 0.729 eV for the HCOO* pathway. The H_2COOH* is the key intermediate of reaction and plays a vital role in the whole reduction process. To further describe the role of H_2COOH*, we drew a schematic diagram of methanol generation by reduction starting with H_2COOH*, as shown in Figure 4.

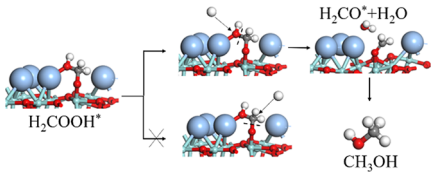

Figure 4. Schematic diagram of methanol generation through H_2COOH* on $Ag_4/(ZrO_2)_9$.

Further hydrogenation of H_2COOH* may break one of the two C−O bonds. Breaking the C−O bond of the O atom bound with the Zr atom will produce CH_3OH* and leave adsorbed O* at the Zr site. Alternatively, breaking the C−O bond away from the catalyst surface results in adsorption of methoxy (CH_3O*) at the Zr site and the formation of H_2O. Subsequently, CH_3O* can be hydrogenated to produce CH_3OH. After the desorption of CH_3OH, the catalyst will return to its original state. It is worth mentioning that, during the calculation, we found it difficult to break the C−O bond of the O atom bound with the Zr atom on $Ag_4/(ZrO_2)_9$, and the reduction product is CH_3OH in both COOH* and HCOO* paths. Previous studies[37,45,46] have shown that CH_3O* is the key intermediate and the oxygen binding of the catalytic site serves as a descriptor to determine the selectivity of the catalyst for CH_4 and CH_3OH. On the $Ag_4/(ZrO_2)_9$ catalyst, the final product was only CH_3OH. It is speculated that the binding ability of O on the catalyst was not strong enough to break the C−O bond on the catalyst, so instead of CH_4, CH_3OH was produced. Similar to $Ag_4/(ZrO_2)_9$, CO_2 reduction paths through COOH* and HCOO* intermediates were studied on $Ag_8/(ZrO_2)_9$. Figure 5 shows the reduction free energy diagram of CO_2 along COOH* and HCOO* pathways and possible intermediates on $Ag_8/(ZrO_2)_9$ at 0 V (RHE).

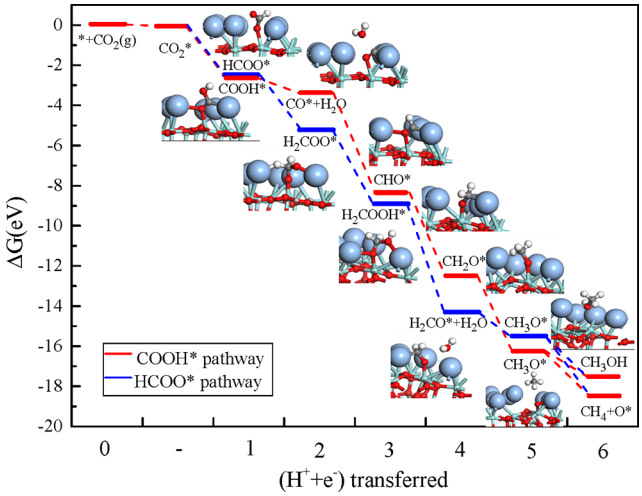

Figure 5. Free energy diagram of CO_2 reduction on $Ag_8/(ZrO_2)_9$ along COOH* and HCOO* pathways at 0 V (RHE). The red line represents the COOH* pathway, and the blue line represents the HCOO* pathway.

The reaction energy of COOH* to form CO* is −2.87 eV on the $Ag_8/(ZrO_2)_9$ surface. Different from the $Ag_4/(ZrO_2)_9$ surface, the reduction products of the $Ag_8/(ZrO_2)_9$ surface in the COOH* path include not only CH_3OH but also CH_4. Compared with the COOH* pathway with a barrier energy of 0.73 eV, the HCOO* pathway with a barrier energy of 0.34 eV provides a lower reaction barrier channel. Therefore, CO_2 will be reduced preferentially through the HCOO* reaction pathway, followed by hydrogenation to H_2COO* and H_2COOH* with 1.73 and 0.78 eV barrier energies, respectively. Finally, the CH_3O* intermediate is reduced to CH_3OH and CH_4. In the HCOO* path, CH_3O* is the key intermediate of the reaction, which directly determines the type of reaction products. The schematic diagram of methanol and methane generation by reduction starting from CH_3O* is shown in Figure 6.

During the hydrogenation of CH_3O*, if the O−Zr bond between CO_2 and the catalyst surface is broken, CH_3OH will

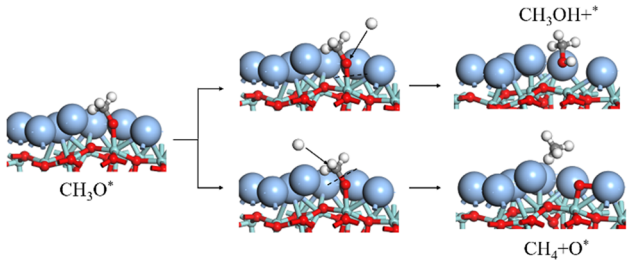

Figure 6. Schematic diagram of methanol and methane generation through CH_3O* on $Ag_8/(ZrO_2)_9$.

https://doi.org/10.1021/acsomega.2c03587
ACS Omega 2022, 7, 34213−34221

be produced. Alternatively, the breaking of the C−O bond in CO_2 leads to the appearance of O* at the Zr site and the formation of CH_4. Then, O* is further hydrogenated to H_2O, and the catalyst is restored to its original state. The barrier energies of the CH_3OH and CH_4 formation were 2.14 and 1.27 eV, respectively. Thermodynamically, the end product is more likely to be CH_4. Based on calculation results on the $Ag_8/(ZrO_2)_9$ catalyst, it is inferred that the O binding ability of the catalyst is stronger than that of $Ag_4/(ZrO_2)_9$. This binding strength can break the C−O bond in CO_2 molecules and finally generate CH_4. According to the data in Table 1, the binding strength of Ag atoms on the $Ag_8/(ZrO_2)_9$ surface is weaker than that on the other two surfaces. This unstable binding may deepen the hybridization between Zr atoms in $Ag_8/(ZrO_2)_9$ and O atoms in CH_3O*, thus enhancing the binding ability of O*.

Similar to the previous two surfaces, CO_2 reduction paths through COOH* and HCOO* intermediates were studied respectively. Figure 7 shows the reduction free energy diagram of CO_2 along COOH* and HCOO* pathways and possible intermediates on $Ag_{12}/(ZrO_2)_9$ at 0 V (RHE).

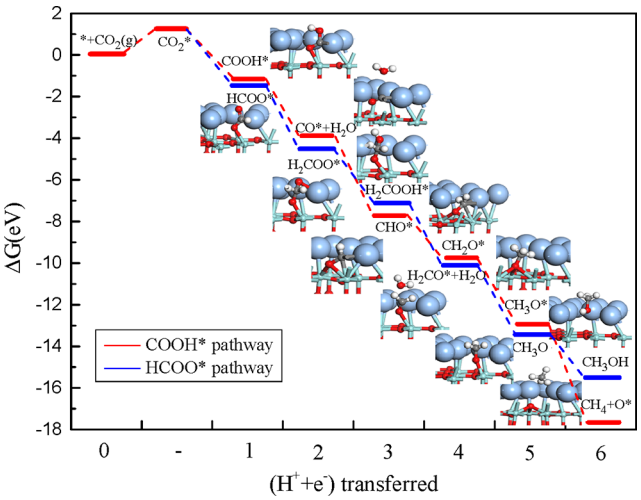

Figure 7. Free energy diagram of CO_2 reduction on $Ag_{12}/(ZrO_2)_9$ along COOH* and HCOO* pathways at 0 V (RHE). The red line represents the COOH* pathway, and the blue line represents the HCOO* pathway.

On the $Ag_{12}/(ZrO_2)_9$ surface, the reaction energy of COOH* forming CO* changes to −2.17 eV and adsorption energy of CO* is −1.38 eV. The reduction product on the $Ag_8/(ZrO_2)_9$ surface through the COOH* path is CH_4. Compared with the COOH* pathway with a barrier energy of 1.47 eV, the HCOO* pathway has a lower barrier energy of 0.19 eV. Therefore, CO_2 will preferentially be reduced through the HCOO* reaction pathway and then continue to hydrogenate to H_2COO* and H_2COOH* with required barrier energies of 0.83 and 0.37 eV, respectively, and finally reduce to CH_3OH. The schematic diagram of the reduction to CH_3OH and CH_4 starting from CH_3O* is shown in Figure 8 with key intermediates in the HCOO* and COOH* path.

Further hydrogenation of CH_3O* breaks the O−Zr bond in the HCOO* path and the C−O bond in the COOH* pathway. The products from COOH* and HCOO* paths are CH_4 and CH_3OH, respectively. In order to qualitatively describe the oxygen binding ability of the catalysts, the PDOS

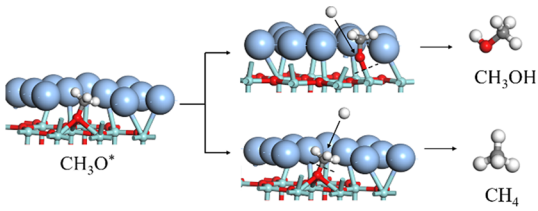

Figure 8. Schematic diagram of methanol and methane generation through CH_3O* on $Ag_{12}/(ZrO_2)_9$.

of the O atoms in the CH_3O* intermediate and the Zr atoms on different surfaces are listed in Figure 9a−c to determine the degree of hybridization of the two atoms. According to Figure 9a,b, the O 2p orbitals of $Ag_4/(ZrO_2)_9$ and $Ag_8/(ZrO_2)_9$ split near the Fermi level, evidencing the formation of new bonding orbitals and antibonding orbitals. The Zr 4d and O 2p orbitals in Figure 9b change in synchrony and coincide better than those in Figure 9a, indicating the deeper and more stable hybridization between Zr and O atoms in $Ag_8/(ZrO_2)_9$ with strong oxygen binding ability.

A schematic diagram containing all C1 intermediates in the reduction process was constructed, as shown in Figure 9d bold arrows are all through HCOO*, but the difference in oxygen binding ability leads to different final products.[47] The $Ag_8/(ZrO_2)_9$ surface has a greater advantage in generating CH_4 due to the stronger oxygen binding ability; the calculated product on the $Ag_4/(ZrO_2)_9$ surface is only CH_3OH with high selectivity; the $Ag_{12}/(ZrO_2)_9$ surface prefers to generate CH_3OH rather than CH_4 from CO_2 reduction. To further illustrate the relation between Ag coverage and oxygen binding ability of the catalyst surface, a schematic diagram was established as shown in Figure 9e. The theoretical study of the Ag dispersion on oxide catalysts can provide the governing principles for experiments. The oxide surfaces with low Ag loading reveal advantages in the formation of CH_3OH, while the medium-Ag coverage surfaces favor CH_4 formation. Besides, the high Ag loading on surfaces reduces the exclusive selectivity for the target product and increases the economic cost of catalysts.

4. CONCLUSIONS

Atomistic-scale models were developed to deliver a functional understanding of catalytic activity and selectivity in the reduction of CO_2 into fuel gases over Ag/ZrO_2 with different dispersion of Ag. By exploring the electronic properties of the Ag/ZrO_2 catalyst with different Ag dispersion, it is found that Ag dispersion affects the electron transfer at the Ag/ZrO_2 interface and the binding strength of Ag atoms, thus changing adsorption properties of CO_2 and electron transport. The higher Ag dispersion increases the number of electrons conducted to CO_2 but decreases the stability of CO_2 adsorption. In the study of CO_2 reduction paths, from the perspective of thermodynamics, the HCOO* path is the dominant reduction path for all three catalysts with different Ag surface dispersion. When the Ag dispersion increases from 25 to 75%, both the reduction path and final product change due to the different binding ability of the catalyst surface with O*. For $Ag_4/(ZrO_2)_9$ and $Ag_{12}/(ZrO_2)_9$, the dominant reduction product is CH_3OH due to its medium binding ability with O*. However, the binding strength of Ag atoms on the $Ag_8/(ZrO_2)_9$ surface is weaker than that on the other two surfaces. This unstable binding may deepen the hybridization

https://doi.org/10.1021/acsomega.2c03587
ACS Omega 2022, 7, 34213−34221

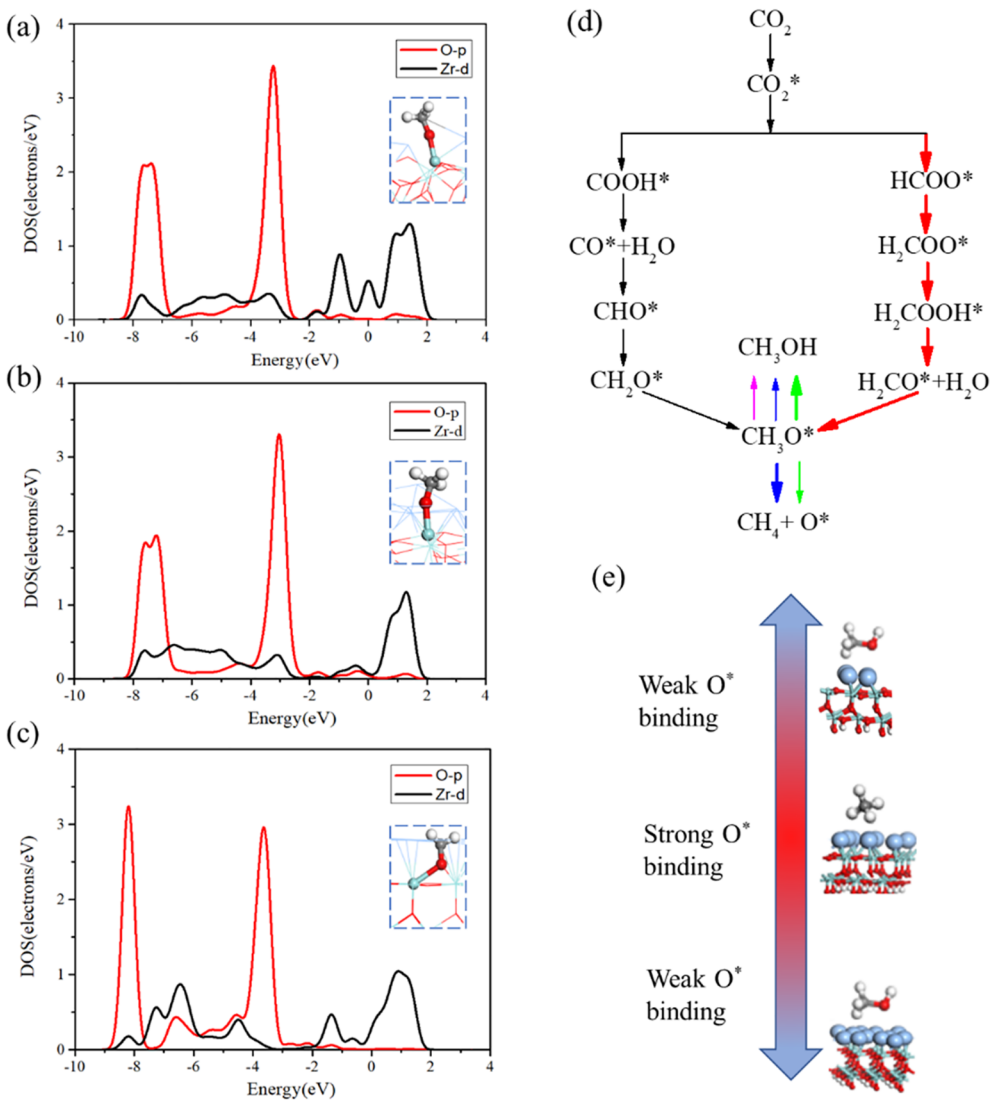

Figure 9. Partial density of states of CH_3O^* on (a) $Ag_4/(ZrO_2)_9$, (b) $Ag_8/(ZrO_2)_9$, and (c) $Ag_{12}/(ZrO_2)_9$; (d) schematic diagram of CH_3OH and CH_4 generation through CH_3O^* on $Ag_4/(ZrO_2)_9$ (in pink), $Ag_8/(ZrO_2)_9$ (in blue), and $Ag_{12}/(ZrO_2)_9$ (in green); and (e) schematic diagram of the relation between Ag coverage and O* binding ability.

between Zr atoms in $Ag_8/(ZrO_2)_9$ and O atoms in CH_3O^*, thus enhancing binding ability of O*. Therefore, the major product of CO_2 reduction on $Ag_8/(ZrO_2)_9$ is CH_4, rather than CH_3OH. In summary, the oxide surfaces with low Ag dispersion reveal advantages in the formation of CH_3OH, while the medium-Ag dispersion surfaces favor CH_4 formation. Besides, the high Ag loading on oxides reduces the stable adsorption of CO_2 and undermines the exclusive selectivity for the target product with higher economic cost of catalysts. Based on the result, tuning the metal/metal oxide interface and interaction by changing the metal dispersion permits the enhancement of CO_2 reduction with precise control of products. The improvement of the catalytic effect which is not determined by a single factor or descriptor requires an in-depth mechanism exploration and experimental study.

■ ASSOCIATED CONTENT

Supporting Information

The Supporting Information is available free of charge at https://pubs.acs.org/doi/10.1021/acsomega.2c03587.

Geometries of Ag_nZrO_2 models; PDOS and spin densities of the Ag_nZrO_2 systems; possible structures of CO_2 adsorption on Ag_nZrO_2 systems with adsorption energies and Mulliken charges; and CO_2 vibrational frequencies in Ag_nZrO_2 systems (PDF)

■ AUTHOR INFORMATION

Corresponding Author

Zongming Zheng − *National Engineering Research Center of New Energy Power Generation, School of New Energy, North China Electric Power University, Beijing 102206, China*; Email: 51101682@ncepu.edu.cn

Authors

Ruonan Duan − *National Engineering Research Center of New Energy Power Generation, School of New Energy, North China Electric Power University, Beijing 102206, China*; orcid.org/0000-0002-7733-0097

Wu Qin − *National Engineering Research Center of New Energy Power Generation, School of New Energy, North China Electric Power University, Beijing 102206, China*

https://doi.org/10.1021/acsomega.2c03587
ACS Omega 2022, 7, 34213−34221

Xianbin Xiao − *National Engineering Research Center of New Energy Power Generation, School of New Energy, North China Electric Power University, Beijing 102206, China*
Bingyun Ma − *National Engineering Research Center of New Energy Power Generation, School of New Energy, North China Electric Power University, Beijing 102206, China*

Complete contact information is available at:
https://pubs.acs.org/10.1021/acsomega.2c03587

Notes

The authors declare no competing financial interest.

■ ACKNOWLEDGMENTS

This work was supported by the National Key R&D Program of China (2021YFE0194500) and the National Natural Science Foundation of China (32171915).

■ REFERENCES

(1) Low, J.; Qiu, S.; Xu, D.; Jiang, C.; Cheng, B. Direct evidence and enhancement of surface plasmon resonance effect on Ag-loaded TiO_2 nanotube arrays for photocatalytic CO_2 reduction. *Appl. Surf. Sci.* **2018**, *434*, 423−432.
(2) Sengupta, A.; Kim, M.; Yoo, C.-S.; Tse, J. S. Polymerization of carbon dioxide: a chemistry view of molecular-to-nonmolecular phase transitions. *J. Phys. Chem. C* **2012**, *116*, 2061−2067.
(3) Kim, K.; Wagner, P.; Wagner, K.; Mozer, A. J. Electrochemical CO_2 reduction catalyzed by copper molecular complexes: the influence of ligand structure. *Energy Fuels* **2022**, *36*, 4653−4676.
(4) De Luna, P.; Hahn, C.; Higgins, D.; Jaffer, S. A.; Jaramillo, T. F.; Sargent, E. H. What would it take for renewably powered electrosynthesis to displace petrochemical processes? *Science* **2019**, *364*, No. eaav3506.
(5) Bushuyev, O. S.; De Luna, P.; Dinh, C. T.; Tao, L.; Saur, G.; van de Lagemaat, J.; Kelley, S. O.; Sargent, E. H. What should we make with CO_2 and how can we make it? *Joule* **2018**, *2*, 825−832.
(6) Hossain, M. D.; Huang, Y.; Yu, T. H.; Goddard III, W. A., III; Luo, Z. Reaction mechanism and kinetics for CO_2 reduction on nickel single atom catalysts from quantum mechanics. *Nat. Commun.* **2020**, *11*, 2256.
(7) Kortlever, R.; Peters, I.; Koper, S.; Koper, M. T. M. Electrochemical CO_2 reduction to formic acid at low overpotential and with high faradaic efficiency on carbon-supported bimetallic Pd-Pt nanoparticles. *ACS Catal.* **2015**, *5*, 3916−3923.
(8) Umeda, M.; Niitsuma, Y.; Horikawa, T.; Matsuda, S.; Osawa, M. Electrochemical reduction of CO_2 to methane on platinum catalysts without overpotentials: strategies for improving conversion efficiency. *ACS Appl. Energy Mater.* **2020**, *3*, 1119−1127.
(9) Xie, S.; Zhang, W.; Lan, X.; Lin, H. CO_2 reduction to methanol in the liquid phase: a review. *ChemSusChem* **2020**, *13*, 6141−6159.
(10) Jiao, S.; Fu, X.; Zhang, L.; Zhang, L.; Ruan, S.; Zeng, Y.-J.; Huang, H. The lab-to-fab journey of copper-based electrocatalysts for multi-carbon production: advances, challenges, and opportunities. *Nano Today* **2021**, *36*, 101028.
(11) Hori, Y.; Katsuhei, K.; Akira, M.; Shin, S. Production of methane and ethylene in electrochemical reduction of carbon dioxide at copper electrode in aqueous hydrogencarbonate solution. *Chem. Lett.* **1986**, *15*, 897−898.
(12) Li, Y.; Sun, Q. Recent advances in breaking scaling relations for effective electrochemical conversion of CO_2. *Adv. Energy Mater.* **2016**, *6*, 1600463.
(13) Ross, M. B.; De Luna, P.; Li, Y.; Dinh, C.-T.; Kim, D.; Yang, P.; Sargent, E. H. Designing materials for electrochemical carbon dioxide recycling. *Nat. Catal.* **2019**, *2*, 648−658.
(14) Feng, Y.; Li, Z.; Liu, H.; Dong, C.; Wang, J.; Kulinich, S. A.; Du, X. Laser-prepared CuZn alloy catalyst for selective electrochemical reduction of CO_2 to ethylene. *Langmuir* **2018**, *34*, 13544−13549.
(15) Feng, R.; Zhu, Q.; Chu, M.; Jia, S.; Zhai, J.; Wu, H.; Wu, P.; Han, B. Electrodeposited Cu-Pd bimetallic catalysts for the selective electroreduction of CO_2 to ethylene. *Green Chem.* **2020**, *22*, 7560−7565.
(16) Wu, Y.; Chen, C.; Yan, X.; Liu, S.; Chu, M.; Wu, H.; Ma, J.; Han, B. Effect of the coordination environment of Cu in Cu_2O on the electroreduction of CO_2 to ethylene. *Green Chem.* **2020**, *22*, 6340−6344.
(17) Chou, T.-C.; Chang, C.-C.; Yu, H.-L.; Yu, W.-Y.; Dong, C.-L.; Velasco-Vélez, J.-J.; Chuang, C.-H.; Chen, L.-C.; Lee, J.-F.; Chen, J.-M.; et al. Controlling the oxidation state of the Cu electrode and reaction intermediates for electrochemical CO_2 reduction to ethylene. *J. Am. Chem. Soc.* **2020**, *142*, 2857−2867.
(18) Tan, X.; Yu, C.; Zhao, C.; Huang, H.; Yao, X.; Han, X.; Guo, W.; Cui, S.; Huang, H.; Qiu, J. Restructuring of Cu_2O to Cu_2O@Cu-metal-organic frameworks for selective electrochemical reduction of CO_2. *ACS Appl. Mater. Interfaces* **2019**, *11*, 9904−9910.
(19) Nam, D. H.; De Luna, P.; Rosas-Hernández, A.; Thevenon, A.; Li, F.; Agapie, T.; Peters, J. C.; Shekhah, O.; Eddaoudi, M.; Sargent, E. H. Molecular enhancement of heterogeneous CO_2 reduction. *Nat. Mater.* **2020**, *19*, 266−276.
(20) Ni, W.; Xue, Y.; Zang, X.; Li, C.; Wang, H.; Yang, Z.; Yan, Y.-M. Fluorine doped cagelike carbon electrocatalyst: an insight into the structure-enhanced CO selectivity for CO_2 reduction at high overpotential. *ACS Nano* **2020**, *14*, 2014−2023.
(21) Xie, J.; Zhao, X.; Wu, M.; Li, Q.; Wang, Y.; Yao, J. Metal-free fluorine-doped carbon electrocatalyst for CO_2 reduction outcompeting hydrogen evolution. *Angew. Chem., Int. Ed.* **2018**, *57*, 9640−9644.
(22) Bandi, A. Electrochemical reduction of carbon dioxide on conductive metallic oxides. *J. Electrochem. Soc.* **1990**, *137*, 2157.
(23) Tan, D.; Zhang, J.; Yao, L.; Tan, X.; Cheng, X.; Wan, Q.; Han, B.; Zheng, L.; Zhang, J. Multi-shelled CuO microboxes for carbon dioxide reduction to ethylene. *Nano Res.* **2020**, *13*, 768−774.
(24) Chu, S.; Yan, X.; Choi, C.; Hong, S.; Robertson, A. W.; Masa, J.; Han, B.; Jung, Y.; Sun, Z. Stabilization of Cu^+ by tuning a CuO-CeO_2 interface for selective electrochemical CO_2 reduction to ethylene. *Green Chem.* **2020**, *22*, 6540−6546.
(25) Hao, L.; Sun, Z. Metal oxide-based materials for electrochemical CO_2 reduction. *Acta Phys. -Chim. Sin.* **2021**, *37*, 2009033.
(26) Chen, Y.; Kanan, M. W. Tin oxide dependence of the CO_2 reduction efficiency on Tin electrodes and enhanced activity for Tin/Tin oxide thin-film catalysts. *J. Am. Chem. Soc.* **2012**, *134*, 1986−1989.
(27) Fan, L.; Fujimoto, K. Promotive SMSI effect for hydrogenation of carbon dioxide to methanol on a Pd/CeO_2 catalyst. *J. Catal.* **1994**, *150*, 217−220.
(28) Graciani, J.; Mudiyanselage, K.; Xu, F.; Baber, A. E.; Evans, J.; Senanayake, S. D.; Stacchiola, D. J.; Liu, P.; Hrbek, J.; Sanz, J. F.; et al. Highly active copper-ceria and copper-ceria-titania catalysts for methanol synthesis from CO_2. *Science* **2014**, *345*, 546−550.
(29) Ma, S.; Lan, Y.; Perez, G. M. J.; Moniri, S.; Kenis, P. J. A. Silver supported on titania as an active catalyst for electrochemical carbon dioxide reduction. *ChemSusChem* **2014**, *7*, 866−874.
(30) Bachiller-Baeza, B.; Rodriguez-Ramos, I.; Guerrero-Ruiz, A. Interaction of carbon dioxide with the surface of zirconia polymorphs. *Langmuir* **1998**, *14*, 3556−3564.
(31) Duyar, M. S.; Gallo, A.; Regli, S. K.; Snider, J. L.; Singh, J. A.; Valle, E.; McEnaney, J.; Bent, S. F.; Rønning, M.; Jaramillo, T. F. Understanding selectivity in CO_2 hydrogenation to methanol for MoP nanoparticle catalysts using in situ techniques. *Catalysts* **2021**, *11*, 143.
(32) Zhu, J.; Ciolca, D.; Liu, L.; Parastaev, A.; Kosinov, N.; Hensen, E. J. M. Flame synthesis of Cu/ZnO-CeO_2 catalysts: synergistic metal-support interactions promote CH_3OH selectivity in CO_2 hydrogenation. *ACS Catal.* **2021**, *11*, 4880−4892.
(33) Inada, Y.; Orita, H. Efficiency of numerical basis sets for predicting the binding energies of hydrogen bonded complexes: evidence of small basis set superposition error compared to gaussian basis sets. *J. Comput. Chem.* **2008**, *29*, 225−232.
(34) Perdew, J. P.; Burke, K.; Ernzerhof, M. Generalized gradient approximation made simple. *Phys. Rev. Lett.* **1996**, *77*, 3865−3868.

(35) Govind, N.; Petersen, M.; Fitzgerald, G.; King-Smith, D.; Andzelm, J. A generalized synchronous transit method for transition state location. *Comput. Mater. Sci.* **2003**, *28*, 250−258.
(36) Nørskov, J. K.; Rossmeisl, J.; Logadottir, A.; Lindqvist, L.; Kitchin, J. R.; Bligaard, T.; Jónsson, H. Origin of the overpotential for oxygen reduction at a fuel-cell cathode. *J. Phys. Chem. B* **2004**, *108*, 17886−17892.
(37) Liang, M.-X.; Zhao, L.; Jia, J.; Wu, H.-S. Au_n (n = 1−16) clusters on the ZrO_2 (111) surface: a DFT+U investigation. *Phys. Chem. Chem. Phys.* **2016**, *18*, 30491−30497.
(38) Chutia, A. A study on the stability of gold copper bimetallic clusters on the CeO_2 (110) surface. *Catal. Commun.* **2022**, *162*, 106376.
(39) Chutia, A.; Willock, D. J.; Catlow, C. R. A. The electronic properties of Au clusters on CeO_2 (110) surface with and without O-defects. *Faraday Discuss.* **2018**, *208*, 123−145.
(40) Osiecki, J. R.; Suto, S.; Chutia, A. Periodic corner holes on the Si (111)-7×7 surface can trap silver atoms. *Nat. Commun.* **2022**, *13*, 2973.
(41) de Souza, E. F.; Appel, L. G. Oxygen vacancy formation and their role in the CO_2 activation on Ca doped ZrO_2 surface: An ab-initio DFT study. *Appl. Surf. Sci.* **2021**, *553*, 149589.
(42) Iyemperumal, S. K.; Deskins, N. A. Activation of CO_2 by supported Cu clusters. *Phys. Chem. Chem. Phys.* **2017**, *19*, 28788−28807.
(43) Sun, K.; Wu, L.; Qin, W.; Zhou, J.; Hu, Y.; Jiang, Z.; Shen, B.; Wang, Z. Enhanced electrochemical reduction of CO_2 to CO on Ag electrocatalysts with increased unoccupied density of states. *J. Mater. Chem. A* **2016**, *4*, 12616−12623.
(44) Rosen, J.; Hutchings, G. S.; Lu, Q.; Rivera, S.; Zhou, Y.; Vlachos, D. G.; Jiao, F. Mechanistic insights into the electrochemical reduction of CO_2 to CO on nanostructured Ag surfaces. *ACS Catal.* **2015**, *5*, 4293−4299.
(45) Bagger, A.; Ju, W.; Varela, A. S.; Strasser, P.; Rossmeisl, J. Electrochemical CO_2 reduction: a classification problem. *ChemPhysChem* **2017**, *18*, 3266−3273.
(46) Mao, X.; Wijethunge, D.; Zhang, L.; Wang, S.; Yan, C.; Zhu, Z.; Du, A. Metal-free graphene/boron nitride heterointerface for CO_2 reduction: surface curvature controls catalytic activity and selectivity. *EcoMat* **2020**, *2*, No. e12013.
(47) Zhai, L.; Cui, C.; Zhao, Y.; Zhu, X.; Han, J.; Wang, H.; Ge, Q. Titania-modified silver electrocatalyst for selective CO2 reduction to CH3OH and CH4 from DFT study. *J. Phys. Chem. C* **2017**, *121*, 16275−16282.

https://doi.org/10.1021/acsomega.2c03587
ACS Omega 2022, 7, 34213−34221